



Effects of the spacing between plasma channels on the fracture behavior of red sandstone under high-voltage pulse discharge

Jiangu Peng · Yuanhang Zhou · Fengpeng Zhang · Jiaqiang Li · Guangliang Yan

Received: 4 January 2024 / Accepted: 2 April 2024
© The Author(s) 2024

Abstract In rock engineering, high-voltage pulse technology has attracted attention because it offers environmental protection, controllable energy, and repeatable discharge. It is necessary to study the fracture behavior of rock under high-voltage pulse discharge (HVPD) for the parametric design of rock breaking thereby. HVPD experiments were conducted in red sandstone samples with the plasma channel spacing ranging from 26 to 66 mm at intervals of 10 mm. The stress wave generated by HVPD was obtained from the current waveform measured by Rogowski coils. In combination with numerical simulations, the distribution characteristics, propagation process, and formation mechanism of fractures were analyzed. The results showed that after two applications of HVPD at different positions, the sample was both broken down and two plasma channels and radial fractures centered around them were formed within. The stress wave decays exponentially with the increase of the distance from the plasma channel. When the spacing between plasma channels is less than or equal to 46 mm, fracture coalescence occurs between the two plasma channels; thereafter,

the fractures formed by the second HVPD face resistance to propagation towards the fracture area formed by the first HVPD. In addition, numerical simulation results indicate that the second HVPD will generate significant tensile stress in the middle region of the two plasma channels, leading to near-horizontal fracture coalescence. When the spacing between plasma channels increases to 56 mm and 66 mm, the tensile stress induced by the second HVPD in the middle region of the sample is small, and it is difficult to form fracture coalescence between the two channels.

Article Highlights

- HVPD experiments with different plasma channel spacings were conducted on sandstone.
- The stress wave generated by HVPD in sandstone was obtained.
- The propagation process of fractures in sandstone induced by HVPD was analyzed.

Keywords High-voltage pulse discharge · Fracture behaviour · Plasma channel · Fracture coalescence

J. Peng · Y. Zhou · F. Zhang (✉) · J. Li
Key Laboratory of Ministry of Education on Safe
Mining of Deep Metal Mines, Northeastern University,
Shenyang 110819, China
e-mail: zhangfengpeng@mail.neu.edu.cn

G. Yan
Benxi Longxin Mining Co., Ltd, Benxi 117013, China

1 Introduction

Fracturing rock is an indispensable process in mining, oil and gas extraction, tunnelling, and other

engineering scenarios. The commonly used explosive blasting and mechanical methods both have some shortcomings. Blasting induces intense vibration, generates toxic gas, causes ejection of debris, and so on (Nateghi 2012; Ghasemi et al. 2013; Bhagat et al. 2021). When the mechanical method represented by TBM encounters hard rock, the tool suffers wear and its efficiency is significantly reduced (Hamidi et al. 2010; Barzegari et al. 2021). Therefore, new rock fracturing techniques are constantly emerging, such as the use of: high-pressure water jetting (Ge et al. 2023), ultrasound (Wang et al. 2022), microwave (Pressacco et al. 2022), laser (Erfan et al. 2017), high voltage pulse (Walsh and Vogler 2020), etc. The high-voltage pulse technique has the advantages of environmental protection, precise adjustment of energy, and efficient treatment of hard rock, which is receiving increasing attention (Andres 2010; Li et al. 2020; Zhu et al. 2020; Ezzat et al. 2022; Liu et al. 2023).

The basis of rock fracturing by HVPD is pulse power technology. Pulse power technology refers to the compression of the primary electrical energy of lower power (10^{-1} MW) and converting it into higher power (10^3 MW) energy through energy storage capacitors and other components for storage, ultimately releasing and acting on the load in an extremely short time. There are two main methods of rock fracturing caused by HVPD: electrohydraulic disintegration and electrical pulse disintegration (Li et al. 2020; Walsh and Vogler 2020; Zhang et al. 2020). In the former, the positive and negative electrodes are placed in the liquid environment, and after discharge, the liquid is broken down to produce shock waves. The shock waves propagate in the liquid and acts on the rock, causing it to break. That is to say, the electrohydraulic disintegration utilizes the compression effect of shock waves. In the latter, the electrodes directly contact the rock, and under the action of discharge, a rapidly expanding plasma channel is formed inside the rock, causing the rock to break under the tensile action of the shock wave. Therefore, the shock wave generated by high-voltage pulse discharge (HVPD) is an important cause of rock fracture.

The microscopic or macroscopic fracturing behavior of rock under external loading is the focus of attention. Fractures usually undergo a process of initiation, propagation, and coalescence (Kong et al. 2022; Zhang et al. 2024). At present, scholars have studied the fracture behavior of rock under the action

of HVPD from different perspectives. Cho et al. (2016) studied the differences of fracture modes by conducting HVPD experiments on circular samples of seven rock types. Zhang et al. (2022) analyzed the spatial distribution characteristics of pore-fracture structure of hard coal samples after being breakdown by HVPD. Bao et al. (2021) found that the discharge voltage can significantly affect the fracturing effect of coal-rock mass. Zhu et al. (2020) conducted electric pulse drilling experiments and found that the rock fracture morphology is related to the formation path of plasma channels. Zhang et al. (2023) discovered the fracture process of rock under the action of HVPD by using high-speed camera. The above achievements provide valuable references to understand the fracture characteristics and mechanisms of rocks under the action of HVPD; however, few of these studies involve the fracturing process prevailing in different fracture zones and the corresponding fracture coalescence.

In engineering practice, it is often necessary to discharge energy at different positions inside the rock to form a larger range of fracture zones. Referring to explosive rock breaking, the spacing between blast holes is a key factor affecting the fragmentation of the rock. When the spacing between two blast holes changes, the rock fragmentation effect will also change accordingly (Li et al. 2017; Drover et al. 2018; Yuan et al. 2019). Therefore, different plasma channels and fracture zones around them will be formed inside the rock under the action of HVPD at different positions. The variation of the spacing between plasma channels will lead to differences in the fracturing effect, making it necessary to study the effect of the spacing between plasma channels on the fracturing behavior; at time of writing, there is a lack of relevant research.

Herein, HVPD experiments with different plasma channel spacings were conducted on red sandstone samples, and the shape and distribution characteristics of the fractures were obtained by an image processing method. The coalescence behavior of the fractures between plasma channels was analyzed. Thereafter, the shock wave formed by the HVPD was calculated through the current waveform, and the dynamic fracture process was simulated by using the finite element modelling. Based on the numerical results, the fracture mechanisms at different plasma channel spacings were investigated.

2 HVPD experiment

2.1 Sample and electrodes

The relatively homogeneous red sandstone was selected as the experimental materials. All samples measuring 250 mm×250 mm×150 mm were cut from the same intact block of red sandstone. The basic physical and mechanical parameters of red sandstone are shown in Table 1. Four circular holes (H1 to H4) with a diameter of 6 mm and a depth of 110 mm were prefabricated on the sample to place the electrodes (Fig. 1a). As shown in Fig. 1b, the electrode is made of copper with good conductivity, and the diameter of the electrode is 4 mm and the length is 200 mm. The electrode is provided with a needle-shaped for forming a discharge plasma channel within the rock. To prevent creep, the electrodes were wrapped with transparent PTFE tube and milky white PTFE tube with good insulation except at the tip.

2.2 Equipment and experimental process

As shown in Fig. 2, the HVPD experimental system is mainly composed of a high-voltage power supply, a MCF140-1 pulse capacitor, a pneumatic trigger switch, a grounding protection switch, and an oscilloscope. The capacitance of the system is 0.994 μF and the maximum output voltage is 120 kV. The oscilloscope is used to record the current waveform collected by the Rogowski coil during HVPD.

The high-voltage pulse discharge experiment was conducted in air. The arrangement of the electrodes in the sample is shown in Fig. 3, and two times of HVPD experiment were carried out in each sample. During the experiment, the tips of the two electrodes were at the same height and in full contact with the hole wall. As shown in Fig. 3b, in hole H1, the electrode tip points towards the positive *x*-axis, while in hole H2, the electrode tip is aligned with the negative *x*-axis. The discharge voltage *U* is 70 kV, the spacing

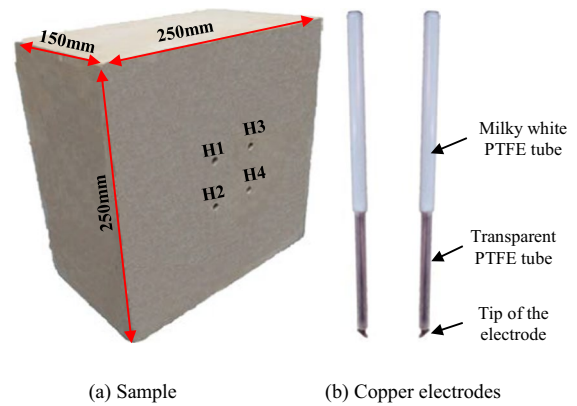


Fig. 1 Sample and electrodes

K between the discharge hole axes is 46 mm, and the discharge depth *H* is 80 mm. The above three parameters are consistent in all experiments. To study the influence of the plasma channel spacing *L* on the rock fracturing effect, five groups of samples with different plasma channel spacings of 26, 36, 46, 56, and 66 mm were designed. These five samples were numbered L26, L36, L46, L56, and L66 mm. It should be noted that the actual plasma channel was mostly curved, which was simplified as a cylinder for the convenience of description.

The two times of HVPD in each sample were conducted separately, and the detailed steps are as follows: (1) Two electrodes are inserted into the holes H1 and H2 respectively, and then connected to the positive and negative electrodes of the HVPD system. (2) The high-voltage power supply is started to charge the MCF140-1 pulse capacitor to store electrical energy. After the charging is completed, the trigger switch is pressed, and the pulse capacitor releases energy, thereby completing a rock fracturing experiment. (3) The grounding switch is pressed to eliminate the residual current in the system. (4) The electrode is inserted into the other two holes H3 and H4, and Steps (1) to (3) are repeated to complete the second rock fracturing experiment. For convenience

Table 1 The basic physico-mechanical parameters of the sample

Density/ kg m ⁻³	Compressive strength/MPa	Tensile strength/MPa	Elastic modulus/ GPa	Poisson's ratio	Wave velocity/m s ⁻¹
2042	74.56	6.02	13.83	0.2119	2249

Fig. 2 The HVPD experimental system

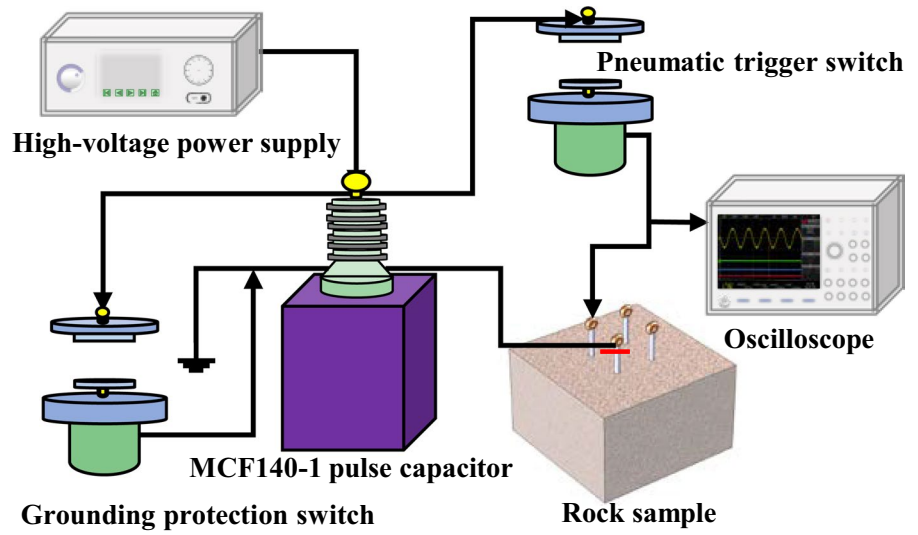
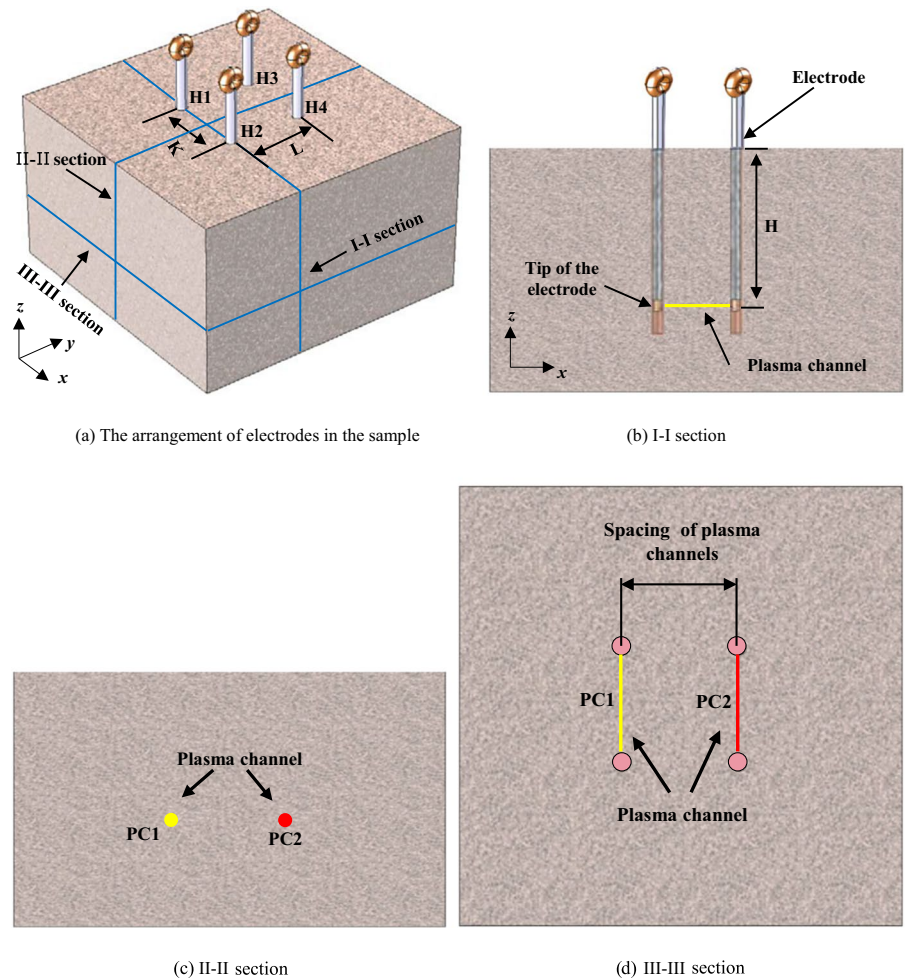


Fig. 3 Experimental scheme of rock fracturing by HVPD



of description, the plasma channel formed by the first HVPD is referred to as plasma channel 1 (PC1), and the plasma channel formed by the second HVPD is referred to as plasma channel 2 (PC2).

3 Experimental results

To study the internal fractures, the sample after HVPD was sectioned and dyed according to the method in the literature (Hamdi et al. 2011; Banadaki and Mohanty 2012). The cutting position is the III-III section shown in Fig. 3d. Subsequently, the stained images were binarized the better to show the morphology of the fractures more clearly.

Figure 4 shows the staining results of fractures in the sample after two times of HVPD under conditions of different plasma channel spacings. Figure 5 shows the corresponding binarization results. As shown in Figs. 4 and 5, the fractures on the left are caused

by the first HVPD, while the fractures on the right are induced by the second HVPD. Under the action of HVPD, radial fractures centered around plasma channels are formed in the sample. In addition, on the profiles of samples L26, L36, and L46, the two fracture zones are connected together. However, two independent fracture zones are formed inside samples L55 and L56 due to the large spacing between PC1 and PC2.

4 Numerical simulation

The HVPD method was used to induce the fracture inside the sample. Due to the non-transparent properties of rock materials, the fracture process of samples could not be observed by high-speed camera or other test methods. The further to explain the experimental results, the LS-DYNA program was used to simulate the dynamic fracture behavior of the sample.

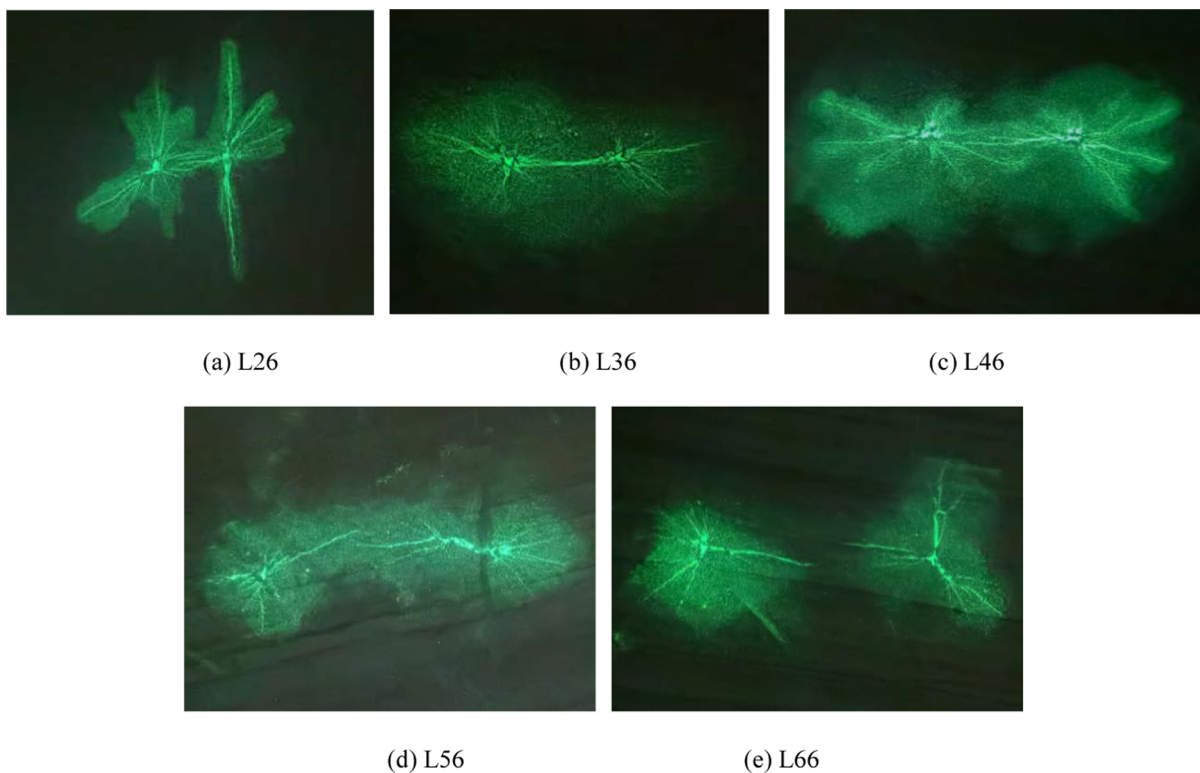
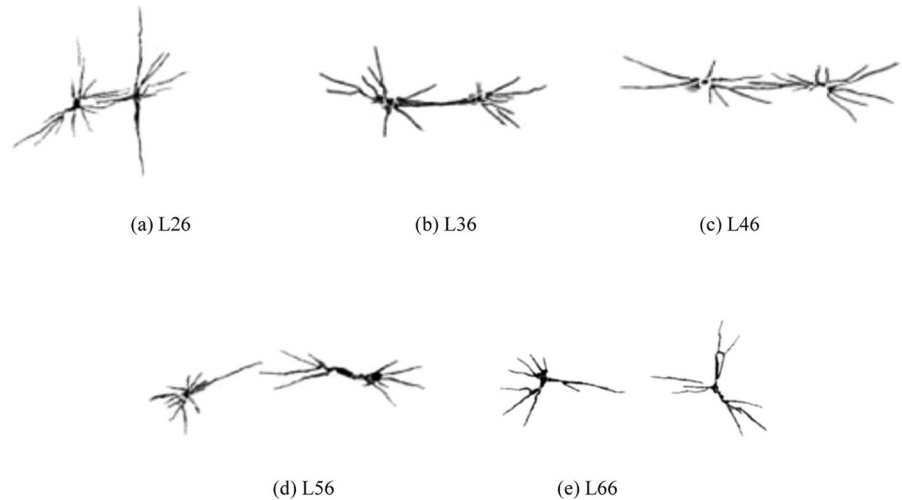


Fig. 4 Staining patterns of fractures in samples with different plasma channel spacings

Fig. 5 Binary patterns of fractures in samples with different plasma channel spacings



4.1 Establishment of finite element model

4.1.1 Geometric model and mesh

To optimize computational efficiency, a half-scale model with dimensions of 125 mm × 250 mm × 150 mm was established (Fig. 6a). The model includes two holes and two plasma channels. The length of the plasma channel is 20 mm, which is half the distance between the discharge points of the two electrodes. As shown in Fig. 6b, hexahedral elements are selected for mesh division. The grid around the holes and plasma channels has been densified, with a minimum grid size of approximately 1 mm. The constraint

in the Y -direction is imposed on the symmetry plane of the model, and the stress wave is imposed on the hole wall of the plasma channels.

4.1.2 Material model

The Riedel Heirmaier Thoma (RHT) model was selected here to simulate fracture behavior under the action of stress waves generated by HVPD. This model introduces the influence of the third invariant of the deviatoric stress tensor on the failure surface, and can comprehensively reflect phenomena such as tensile and compressive damage, strain rate effects, etc. of the material (Hallquist 2006). According to previous

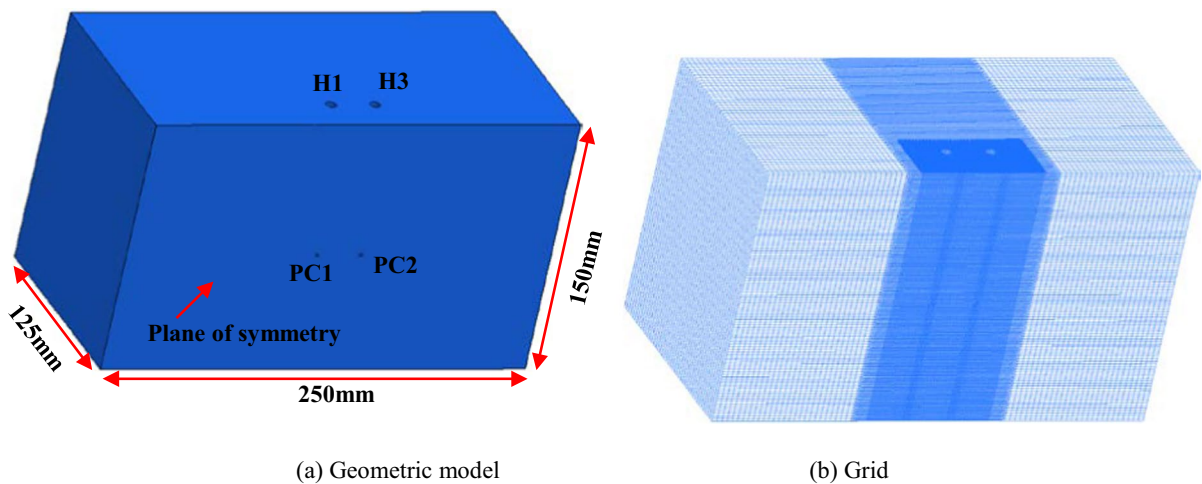


Fig. 6 Geometric model and meshing

literature, it has been successfully applied to study the damage and fracture behavior of rock materials under dynamic loads such as explosion and impact (Jayasinghe et al. 2019; Li et al. 2023). The main parameters of the rock sample are shown in Table 2.

4.1.3 Stress waves

In the process of rock fracturing by HVPD, the current is injected into the rock through the positive electrode, and then enters the negative electrode after passing through the rock, forming a complete current loop (Burkin et al. 2009; Kang et al. 2023). Based on the Kirchhoff loop equation, the following equivalent discharge loop model equation can be established:

$$\begin{aligned}
 & i(t) \times K_{td} \times l_{td} \times \left(\int_0^t i(t)^2 dt \right)^{-1/2} \\
 & + \frac{1}{C} \times \int_0^t i(t) dt - U_0 \\
 & + \left[R_1 + (R_0 - R_1) \times e^{-t/Q_R} \right] \\
 & \times i(t) + L \times \frac{di(t)}{dt} = 0
 \end{aligned} \tag{1}$$

where i is the current, R_0 is the initial resistance of the circuit, R_1 denotes the limiting minimum resistance, Q_R is the time constant of the resistance drop, L represents the inductance, K_{td} is the resistivity, l_{td} is the length of the plasma channel, and C is the capacitance.

The resistance $R_{td}(t)$ of the plasma channel is expressed in the form of current integration as follows:

$$R_{td}(t) = \frac{K_{td} \times l_{td}}{\sqrt{\int_0^t i^2(t) dt}} \tag{2}$$

The energy W_{td} injected into the plasma channel is calculated as follows:

$$W_{td}(t) = \int_0^t i^2(t) \times R_{td}(t) dt \tag{3}$$

In the process of rock fracturing by HVPD, part of the energy injected into the plasma channel is used to heat the plasma channel, and the other part is adopted to expand the plasma channel to form a shock wave (Burkin et al. 2009; Kang et al. 2023):

Table 2 Parameters of the RHT model

Parameter	Value	Parameter	Value
Mass density RO (kg/m ³)	2042	Porosity exponent NP	3.0
Initial porosity ALPHA	1.06	Reference compressive strain rate EOC	3.0E−8
Crush pressure PEL (MPa)	24.8	Reference tensile strain rate EOT	3.0E−9
Compaction pressure PCO (GPa)	6.0	Break compressive strain rate EC	3.0E22
Hugoniot polynomial coefficient A ₁ (GPa)	8.0014	Break tensile strain rate ET	3.0E22
Hugoniot polynomial coefficient A ₂ (GPa)	13.4424	Compressive strain rate dependence exponent BETAC	0.016427
Hugoniot polynomial coefficient A ₃ (GPa)	8.2159	Tensile strain rate dependence exponent BETAT	0.021116
Parameter for polynomial EOS B ₀	1.22	Volumetric plastic strain fraction in tension PTF	0.001
Parameter for polynomial EOS B ₁	1.22	Compressive yield surface parameter GC*	0.53
Parameter for polynomial EOS T ₁	8.0014	Tensile yield surface parameter GT*	0.7
Parameter for polynomial EOS T ₂	0.0	Erosion plastic strain EPSF	2.0
Elastic shear modulus SHEAR (GPa)	5.706	Shear modulus reduction factor XI	0.5
Compressive strength FC (MPa)	74.56	Damage parameter D1	0.04
Relative tensile strength FT*	0.0808	Damage parameter D2	1.0
Relative shear strength FS*	0.15	Minimum damaged residual strain EPM	0.01
Failure surface parameter A	1.6	Residual surface parameter AF	1.6
Failure surface parameter N	0.61	Residual surface parameter AN	0.61
Lode angle dependence factor Q ₀	0.6805	Gruneisen gamma GAMMA	0.0
Lode angle dependence factor B	0.0105		

$$\frac{dW_{td}}{dt} = \frac{P \times dV_{td}}{dt} + \frac{1}{\gamma - 1} \frac{d(PV_{td})}{dt} \quad (4)$$

where P is the stress wave; V_{td} stands for the plasma channel volume; γ is the isentropic index.

The stress wave P generated by the expansion of the plasma channel is represented as follows:

$$P(t) = \frac{\gamma - 1}{V_{td} \times \gamma} W_{td} \quad (5)$$

The plasma channel can usually be simplified as a cylinder, therefore, the expression for V_{td} is as follows:

$$V_{td} = \pi r_{td}^2(t) l_{td} \quad (6)$$

where r_{td} is the radius of the plasma channel.

V_{td} can be solved using the Euler method:

$$\begin{aligned} \frac{dV_{td}}{dt} = & \left(\frac{\sqrt{7}\alpha^{1/14}}{3\sqrt{\rho_0}} \right) \\ & \times \left[\left(\frac{W_{td}}{V_{td}} \times \frac{\gamma - 1}{\gamma} + \beta \right)^{3/7} - \beta^{3/7} \right] \\ & \times \left(\sqrt{\frac{V_{td}}{\pi l_{td}}} \times 2\pi l_{td} \right) \end{aligned} \quad (7)$$

where α and β are the impact coefficients; ρ_0 is the density.

The current monitored by the Rogowski coil sensor during the experiment is shown in Fig. 7. The current increases rapidly from 0 to a peak value of 19.8 kA and then decays to 0 in an oscillating manner. According to formulae 1 to 7, the stress wave used in the numerical simulation described herein can be obtained (Fig. 8). It can be seen that the amplitude of the stress wave is 201.97 MPa. During the experiment, the second HVPD was applied after the first HVPD was completed and the residual current was eliminated, and the time interval between the two HVPDs was long. To give consideration to the calculation efficiency, the time interval between the stress waves being applied to the walls of PC1 and PC2 is set to 200 μ s by trial calculation.

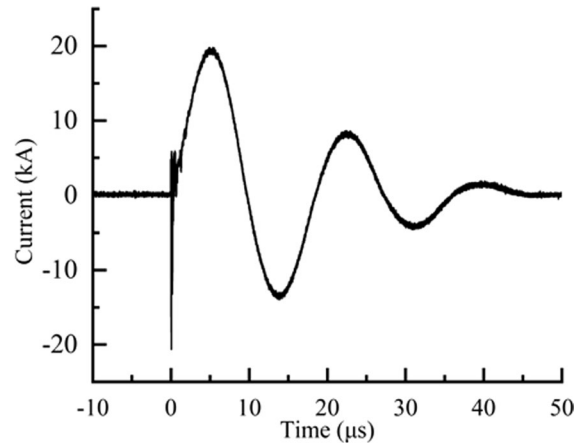


Fig. 7 Time history curve: current

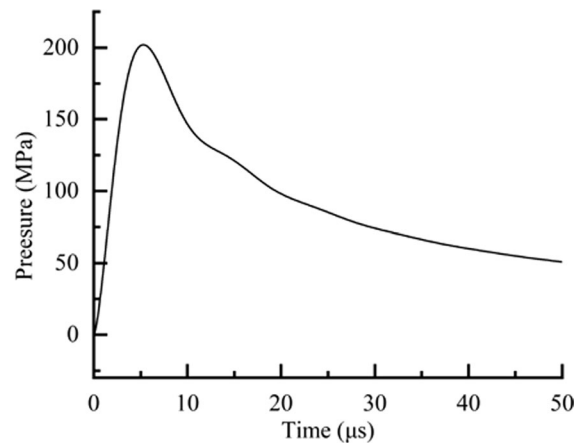


Fig. 8 Time history curve: the shock wave

4.2 Numerical simulation results

4.2.1 Attenuation of stress waves

To study the attenuation of the stress wave of HVPD, the sample L26 is taken as an example. Seven points (A-G) at the bottom left of PC1 were selected. The first monitoring point A on the lower left was located at a distance of 2.5 mm from the wall of PC1, and the remaining six monitoring

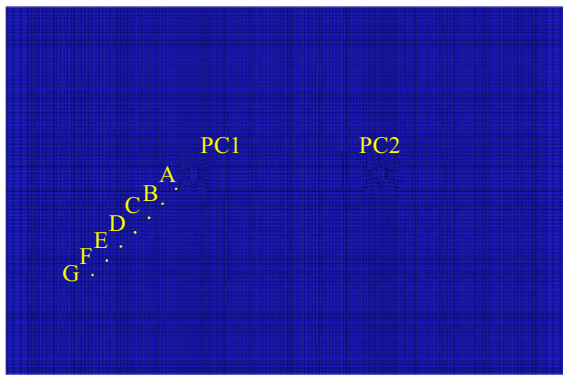


Fig. 9 Location of monitoring points

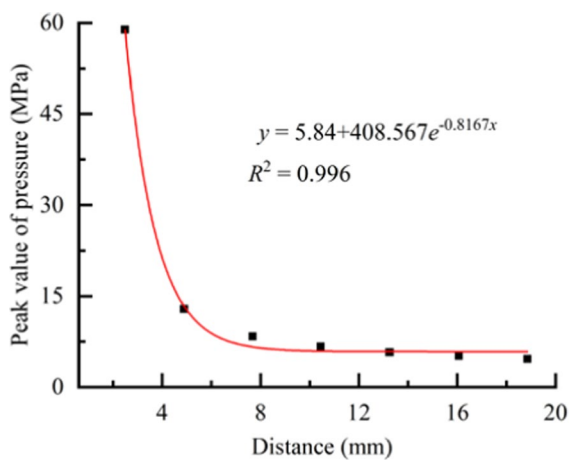


Fig. 10 Attenuation of stress wave of HVPD with distance

points were spaced at equal intervals of 2.8 mm (Fig. 9). The pressure time history curves of these monitoring points were extracted to obtain the peak values. Figure 10 shows the variations of the peak pressure with distance. The peak values corresponding to seven points are 58.9, 12.9, 8.3, 6.7, 5.7, 5.1 and 4.6 MPa, respectively. In other words, the peak value of the stress wave formed by the HVPD shows a non-linear decreasing trend with increasing distance. According to the simulation results, a negative exponential function is used to fit the attenuation of stress waves, with a fitting variance of 0.996.

4.2.2 Dynamic fracturing process

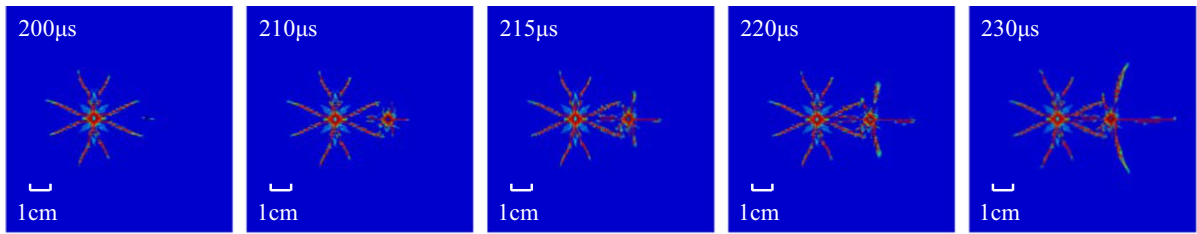
In agreement with the previous experiments, numerical simulations were conducted to represent different

plasma channel spacings. The morphology of the fracture network around the PC1 is similar under different plasma channel spacings, therefore, only the fracture propagation process corresponding to PC2 is shown (Fig. 11a–e). As shown in Fig. 11a that, at 210 μ s, radial fractures develop around the PC2 in the sample L26; at 215 μ s, the fractures formed by two HVPDs are connected; after that, it is difficult for the radial fractures to continue to expand to the left. In Fig. 11b, at 210 μ s, radial fractures at the periphery of PC2 in sample L36 propagates outward; at 215 μ s, the fractures tend to propagate to the left; in addition, a nearly horizontal fracture appears near PC2 and propagates to the left; At 220 μ s, the fractures in the two fracture zones are connected, and the connection time is delayed compared with that of sample L26; at 230 μ s, the fractures propagating to the left side tend to stop developing, and the length of the remaining fractures is further increased. As illustrated in Fig. 11c, at 215 μ s, a horizontal fracture propagating to the left side begins to appear near the PC2. This is similar to sample L36; at 230 μ s, the fracture zones formed by two HVPDs are connected together. As the distance between the two plasma channels further increases, eight main fractures appear around the PC2 in samples L56 and L66 and continue to expand outward. However, no fractures propagating in the horizontal direction occurred in these two samples (Fig. 11d, e).

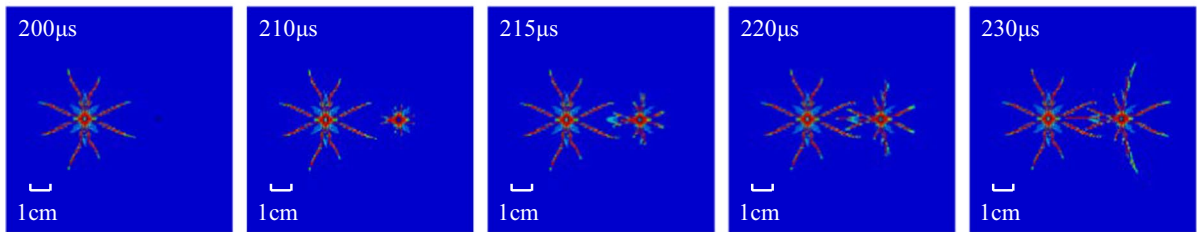
The aforementioned results show that the plasma channel spacing significantly affects the fracture propagation process under the second HVPD. With the increase of the spacing between plasma channels, the fracture coalescence becomes more difficult. In addition, due to the influence of the first HVPD, when the spacing between plasma channels is less than or equal to 46 mm, the fracture formed by the second HVPD is difficult to continue to expand to the left after the two fracture zones are connected.

4.2.3 Comparison of numerical simulation and experimental results

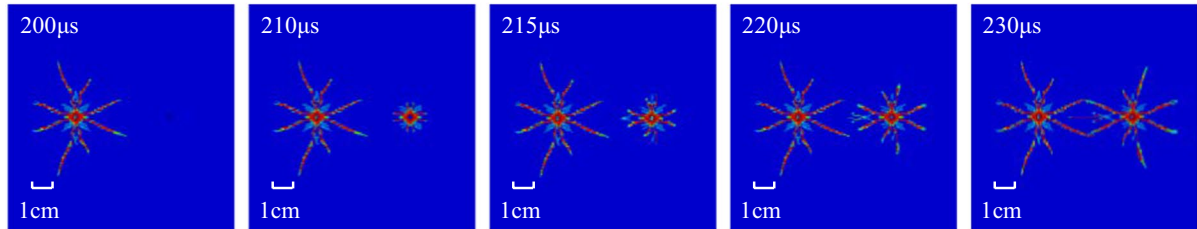
Figure 12 shows a comparison between experimental and numerical simulation results. The fractures obtained by numerical simulation are radial, and the morphology of the fracture network is consistent with the experimental results. In addition, the fracture coalescence behavior at different channel spacings also matches the experiment. When the spacing between



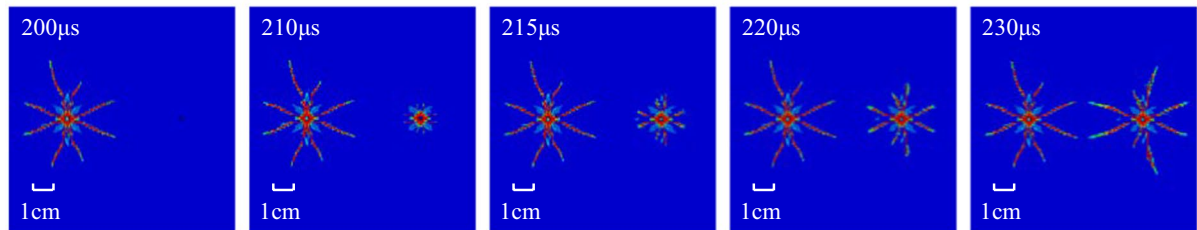
(a) L26



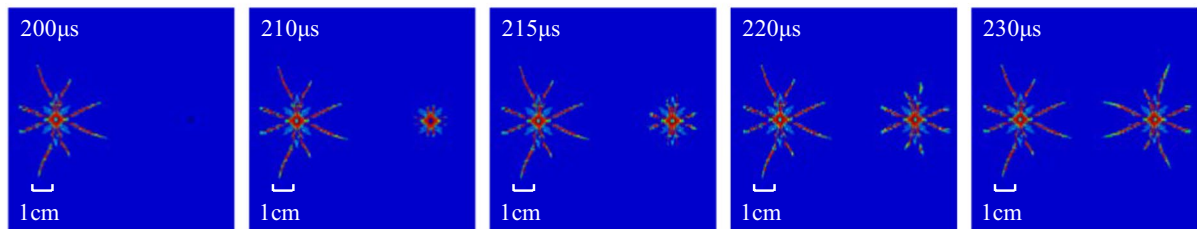
(b) L36



(c) L46



(d) L56



(e) L66

Fig. 11 The fracture process of samples induced by HVPD at different plasma channel spacings

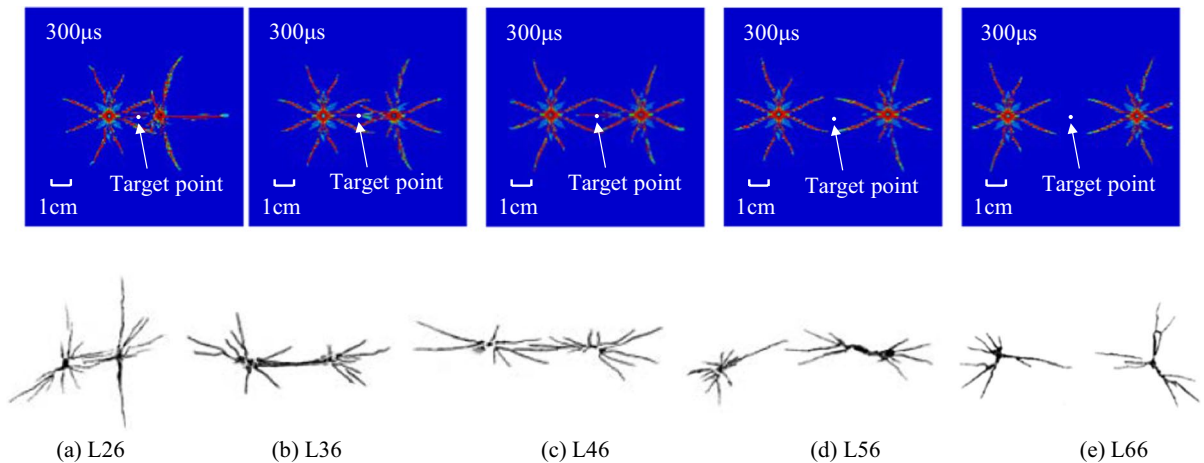


Fig. 12 Comparison between simulation results and experimental results

plasma channels is less than or equal to 46 mm, the fracture zones formed by two HVPDs are connected. As the spacing between plasma channels increases, the two fracture zones are mutually independent. From the numerical simulation results, the fracture morphology of the two independent fracture zones is quasi-symmetrical, while the experimental results are not completely symmetrical. In general, the numerical simulation results are in good agreement with the experimental results, but slightly different. This difference is mainly attributed to the following reasons: one of the reasons is the influence of load. In the simulation, the stress wave is directly used to load the sample, however, in the process of electrical breakdown of the rock, it will also be affected by high temperature, even if the range of influence of high temperatures is limited. Another reason is the difference in the shape of the plasma channel, because the real plasma channel formed inside the rock is actually curved and its interface is not ideally circular due to the influence of the internal microstructure of the rock; however, the plasma channel in the numerical simulation is simplified to an ideal cylinder.

5 Discussion

In the process of rock fracturing by HVPD, the pulse voltage is first applied to the high and low-voltage electrodes. Then, a dendritic discharge leader is formed inside the rock near the high-voltage

electrode, and its trunk extends continuously to reach the low-voltage electrode, thus forming a plasma channel through the two electrodes (Li et al. 2020; Zhang et al. 2020). That is to say, a complete discharge circuit is generated. Thereafter, the capacitor discharges its stored electrical energy. A portion of the total electrical energy is converted to resistive loss energy in the circuit, and another portion is released into the plasma channel. The energy injected into the plasma channel is converted into plasma channel heating energy and plasma channel expansion energy to form a shock wave (Burkin et al. 2009). The shock wave generated by high-voltage pulse discharge will form a tangential tensile stress when it propagates outward from the plasma channel. This tangential tensile stress exceeds the tensile limit of red sandstone. Therefore, several radial fractures are produced in the sample under the action of tangential tensile load (Fig. 11).

The further to elucidate the formation mechanism of fractures between channels, the target points were selected near the middle of the two channels and the pressure time history curves were extracted (Fig. 12). Figure 13 shows the time-history curve of pressure of the target points at different plasma channel spacings. It can be seen that under the first HVPD, the stress wave of these target points is mainly compressive, and the peak value of the stress wave decreases with the increase in the spacing between plasma channels. After the first HVPD, a radial fracture zone with PC1 at its center is formed (Fig. 11), which will lead to

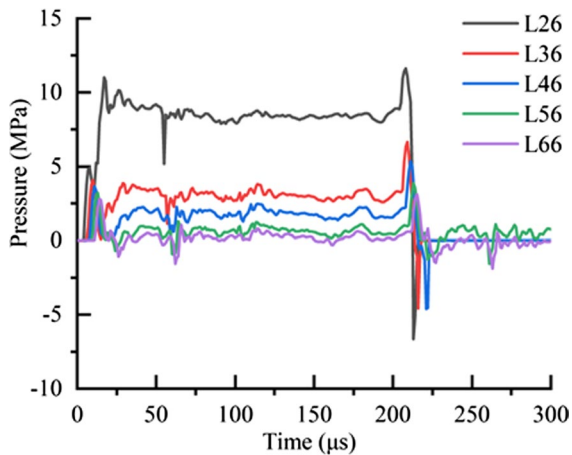


Fig. 13 Pressure time history curves at target points

the change of the stress state at the target point under the second HVPD. As shown in Fig. 13, after 200 μs , under the action of the second HVPD, the target points of specimens L26, L36, and L46 have a larger tensile peak value, and the rock is more prone to fracture under the action of tensile load. On the other hand, the tensile peak values at the target points of samples L56 and L66 are smaller. This is due to the fact that with the increase in the spacing between plasma channels, the influence of the fracture zone formed by the first HVPD on the second HVPD is weakened. Besides, the target points are relatively far from the center of the plasma channel. It can be seen from the simulation results in Fig. 10 that the pressure peak demonstrates a feature of rapid decay with increasing distance. Therefore, the pressure peaks in Fig. 13 are much lower than those in Fig. 8.

6 Conclusion

The fracture morphology and coalescence behavior of red sandstone samples with different plasma channel spacings were studied by HVPD experiments. In addition, the attenuation law of stress wave was analyzed by numerical simulations, the dynamic fracture process of the sample was reproduced, and the mechanism of fracture coalescence was revealed. The main conclusions are as follows:

1. Under the action of two times of HVPD, two radial fracture zones centered on plasma channels

were formed inside the red sandstone. The spacing between plasma channels affects the propagation of fractures. When the spacing is small, the fracture of the first HVPD prevents the radial fracture of the second HVPD from propagating to the left. When the spacing is greater than 46 mm, the two fracture regions are quasi-independent of each other.

2. Based on the monitored current waveform and combined with theoretical analysis, the time-history curve of stress wave of HVPD was plotted. The results show that the stress wave of HVPD attenuates exponentially with the increase of distance in the red sandstone sample.
3. The spacing between plasma channels affects the fracture coalescence behavior. Under the condition of small distance, a nearly horizontal fracture appears in the middle of the two plasma channels. The second HVPD can form a large tensile load in the middle of the two plasma channels, which leads to the formation of horizontal through fractures. As the spacing increases, it becomes difficult to form fracture coalescence between plasma channels.

Author contributions PJ wrote the main manuscript text. ZY and LJ prepared all the figures in the manuscript. ZF designed the experimental scheme. ZY, LJ and YG processed all the data in the manuscript. All authors reviewed the manuscript.

Funding This work was supported by the National Natural Science Foundation of China (Grant No. 52104119).

Data availability Data will be made available on request.

Declarations

Conflict of interest The authors declare that they have no competing interests.

Ethics approval The authors declare that the submitted work is original and has not been submitted to more than one journal for simultaneous consideration.

Consent to publish All authors agree to publish this manuscript in the journal.

Open Access This article is licensed under a Creative Commons Attribution 4.0 International License, which permits use, sharing, adaptation, distribution and reproduction in any medium or format, as long as you give appropriate credit to the original author(s) and the source, provide a link to the Creative

Commons licence, and indicate if changes were made. The images or other third party material in this article are included in the article's Creative Commons licence, unless indicated otherwise in a credit line to the material. If material is not included in the article's Creative Commons licence and your intended use is not permitted by statutory regulation or exceeds the permitted use, you will need to obtain permission directly from the copyright holder. To view a copy of this licence, visit <http://creativecommons.org/licenses/by/4.0/>.

References

- Andres U (2010) Development and prospects of mineral liberation by electrical pulses. *Int J Miner Process* 97(1–4):31–38. <https://doi.org/10.1016/j.minpro.2010.07.004>
- Banadaki MMD, Mohanty B (2012) Numerical simulation of stress wave induced fractures in rock. *Int J Impact Eng* 40–41:16–25. <https://doi.org/10.1016/j.ijimpeng.2011.08.010>
- Bao XK, Guo JY, Liu Y, Zhao G, Cao JX, Wu JW, Zhao JC (2021) Damage characteristics and laws of micro-crack of underwater electric pulse fracturing coal-rock mass. *Theor Appl Fract Mech* 111:102853. <https://doi.org/10.1016/j.tafmec.2020.102853>
- Barzegari G, Khodayari J, Rostami J (2021) Evaluation of TBM cutter wear in naghadeh water conveyance tunnel and developing a new prediction model. *Rock Mech Rock Eng* 54(12):6281–6297. <https://doi.org/10.1007/s00603-021-02640-7>
- Bhagat NK, Rana A, Mishra AK, Singh MM, Singh A, Singh PK (2021) Prediction of fly-rock during boulder blasting on infrastructure slopes using CART technique. *Geomat Nat Haz Risk* 12(1):1715–1740. <https://doi.org/10.1080/19475705.2021.1944917>
- Burkin VV, Kuznetsova NS, Lopatin VV (2009) Dynamics of electro burst in solids: I. Power characteristics of electro burst. *J Phys D Appl Phys* 42(18):185–204. <https://doi.org/10.1088/0022-3727/42/18/185204>
- Cho SH, Cheong SS, Yokota M, Kaneko K (2016) The dynamic fracture process in rocks under high-voltage pulse fragmentation. *Rock Mech Rock Eng* 49(10):3841–3853. <https://doi.org/10.1007/s00603-016-1031-z>
- Drover C, Villaescusa E, Onederra I (2018) Face destressing blast design for hard rock tunnelling at great depth. *Tunn Undergr Sp Tech* 80:257–268. <https://doi.org/10.1016/j.tust.2018.06.021>
- Erfan MR, Shahriar K, Sharifzadeh M, Ahmadi M, Torkamany MJ (2017) Moving perforation of rocks using long pulse Nd:YAG laser. *Opt Laser Eng* 94:12–16. <https://doi.org/10.1016/j.optlaseng.2017.02.010>
- Ezzat M, Adams BM, Saar MO, Vogler D (2022) Numerical modeling of the effects of pore characteristics on the electric breakdown of rock for plasma pulse geo drilling. *Energies* 15(1):250. <https://doi.org/10.3390/en15010250>
- Ghasemi E, Ataei M, Hashemolhosseini H (2013) Development of a fuzzy model for predicting ground vibration caused by rock blasting in surface mining. *J Vib Control* 19(5):755–770. <https://doi.org/10.1177/1077546312437002>
- Ge ZL, Zhang HW, Zhou Z, Cao SR, Zhang D, Liu XJ, Tian C (2023) Experimental study on the characteristics and mechanism of high-pressure water jet fracturing in high-temperature hard rocks. *Energy* 270:126848. <https://doi.org/10.1016/j.energy.2023.126848>
- Hallquist JO (2006) *Ls-dyna theory manual*.
- Hamdi E, Romdhane NB, Le Cleac'h JM (2011) A tensile damage model for rocks: application to blast induced damage assessment. *Comput Geotech* 38(2):133–141. <https://doi.org/10.1016/j.compgeo.2010.10.009>
- Hamidi JK, Shahriar K, Rezai B, Rostami J (2010) Performance prediction of hard rock TBM using rock mass rating (RMR) system. *Tunn Undergr Sp Tech* 25(4):333–345. <https://doi.org/10.1016/j.tust.2010.01.008>
- Jayasinghe LB, Shang JL, Zhao ZY, Goh ATC (2019) Numerical investigation into the blasting-induced damage characteristics of rocks considering the role of in-situ stresses and discontinuity persistence. *Comput Geotech* 116:103207. <https://doi.org/10.1016/j.compgeo.2019.103207>
- Kang JF, Li CP, Duan LC, Xiao YB, Li A (2023) An experimental and numerical study on the mechanism of high-voltage electro pulse rock-breaking. *Rock Mech Rock Eng* 56:2185–2195. <https://doi.org/10.1007/s00603-022-03154-6>
- Kong L, Ranjith PG, Li QB, Song Y (2022) Rock grain-scale mechanical properties influencing hydraulic fracturing using Hydro-GBM approach. *Eng Fract Mech* 262:108227. <https://doi.org/10.1016/j.engfracmech.2021.108227>
- Li XP, Huang JH, Luo Y, Chen PP (2017) A study of smooth wall blasting fracture mechanisms using the timing sequence control method. *Int J Rock Mech Min Sci* 92:1–8. <https://doi.org/10.1016/j.ijrmms.2016.12.001>
- Li YS, Liu J, Feng BY, Zhang XR, Zhang MY, Xiao HL, He MB, Shi FN (2020) Numerical modeling and simulation of the electric breakdown of rocks immersed in water using high voltage pulses. *Geomech Geophys Geo-energ Geo-resour*. <https://doi.org/10.1007/s40948-020-00190-w>
- Li XD, Liu KW, Qiu T, Sha YY, Yang JC, Song RT (2023) Numerical study on fracture control blasting using air-water coupling. *Geomech Geophys Geo-energ Geo-resour*. <https://doi.org/10.1007/s40948-023-00546-y>
- Liu WJ, Hu H, Zhu XH, Luo YX, Chen MQ (2023) The fragmentation mechanism of granite in electrical breakdown process of plasma channel drilling. *Geomech Geophys Geo-energ Geo-resour*. <https://doi.org/10.1007/s40948-023-00550-2>
- Nateghi R (2012) Evaluation of blast induced ground vibration for minimizing negative effects on surrounding structures. *Soil Dyn Earthq Eng* 43:133–138. <https://doi.org/10.1016/j.soildyn.2012.07.009>
- Pressacco M, Kangas JJJ, Saksala T (2022) Numerical modelling of microwave heating assisted rock fracture. *Rock Mech Rock Eng* 55(2):481–503. <https://doi.org/10.1007/s00603-021-02685-8>
- Walsh SDC, Vogler D (2020) Simulating electropulse fracture of granitic rock. *Int J Rock Mech Min Sci* 128:104238. <https://doi.org/10.1016/j.ijrmms.2020.104238>

- Wang HJ, Li HZ, Tang L, Li JC, Ren XH (2022) Fracturing behavior of brittle solids containing 3D internal crack of different depths under ultrasonic fracturing. *Int J Min Sci Technol* 32(6):1245–1257. <https://doi.org/10.1016/j.ijmst.2022.09.008>
- Yuan W, Liu SG, Wang W, Su XB, Li ZH, Li JX, Wen L, Chang JF, Sun XY (2019) Numerical study on the fracturing mechanism of shock wave interactions between two adjacent blast holes in deep rock blasting. *Earthq Eng Eng Vib* 18(4):735–746. <https://doi.org/10.1007/s11803-019-0533-6>
- Zhang XL, Lin BQ, Li YJ, Zhu CJ (2020) Experimental study on the effect of coal thickness and breakdown voltage on energy conversion during electrical disintegration. *Fuel* 259:116135. <https://doi.org/10.1016/j.fuel.2019.116135>
- Zhang XL, Lin BQ, Shen J (2022) Quantitative analysis on pore-fracture structure induced by plasma breakdown based on CT scanning. *Eng Fract Mech* 273:108756. <https://doi.org/10.1016/j.engfracmech.2022.108756>
- Zhang ZH, Nie BS, Hou YA, Wang YJ, Li XC, Meng JQ, Liu XF (2023) Characteristics investigation on shock wave fracture rock based on Hilbert–Huang transform method using large-scale electric explosion tests. *Powder Technol* 415:118202. <https://doi.org/10.1016/j.powtec.2022.118202>
- Zhang DC, Lu GJ, Song YQ, Nie W, Ranjith PG (2024) Experimental study of the effect of ultralow temperature on the fracture toughness of sandstone. *Eng Fract Mech* 296:109830. <https://doi.org/10.1016/j.engfracmech.2023.109830>
- Zhu XH, Luo YX, Liu WJ (2020) On the rock-breaking mechanism of plasma channel drilling technology. *J Petrol Sci Eng* 194:107356. <https://doi.org/10.1016/j.petrol.2020.107356>

Publisher's Note Springer Nature remains neutral with regard to jurisdictional claims in published maps and institutional affiliations.